Investigating liquid-fronts during spontaneous imbibition of liquids in industrial wicks.

Part II: Validation by DNS

M. Amin F. Zarandi, Krishna M Pillai[1], Abul Borkot Md Rafiqul Hasan

Laboratory for Flow and Transport Studies in Porous Media

Dept. of Mechanical Engineering, University of Wisconsin- Milwaukee, Milwaukee, WI 53211

ABSTRACT

To validate the experimental results of Part-1, we conducted a two-phase flow simulation of imbibition of a wetting liquid through 2D microstructures made of ellipses of varying aspect ratios. The flow simulation in the particulate microstructures, characterized by low (ellipse) aspect ratio, produced somewhat even micro-fronts, thus replicating the sharp fronts at the visual (macroscopic) scale observed in Part-1. Whereas simulations in the fibrous microstructures produced highly uneven micro-fronts, suggesting the formation of semi-sharp or diffuse visual fronts. Increasing the porosity from 50% to 70% resulted in solid-phase clustering and led to further increase in the unevenness of micro-fronts, pointing to purely diffuse visual fronts. The evolution of the saturation plots along the flow direction, obtained from area-averaging of fluid-distribution plots, pointed to diffusing of sharp fronts with time. The predictions matched our previous experimental and numerical observations, i.e., the particulate media create sharp fronts while the fibrous media create semi-sharp/diffuse fronts.

[1] Corresponding author

Keywords: porous wicks, wicking, sharp-front model, Richards equation, unsaturated flow

1. INTRODUCTION

During the wicking process, which is defined as the invasion of a wetting liquid into a dry porous medium, the liquid (the wetting phase) displaces air (the non-wetting phase) from the pores of the wicks thus ensuring partial or full saturation. During this imbibition process, the liquid front at the pore (micro) level acts as the interface between the liquid and air phases. In some previous studies, the wettability has been measured through the rate of advance of a liquid front [1, 2]. There have been some investigations that focused on finding different parameters affecting the wicking process and thus evaluate the sensitivity of liquid front to these parameters. We are going to detail some of these efforts below.

Hu et al [2] conducted a quantitative analysis based on a pore-scale simulation and investigated the transition of liquid fronts form from fingering to stable flow under the effect of wettability. They suggested that the progress of the liquid front slows down under reduced wettability conditions. Zhang et al [3]. conducted a series of displacement experiments and concluded that the front shape is highly dependent on different parameters such as the capillary number, viscosity ratio, and the heterogeneity of the porous medium. Bakhshian et al [4] simulated the front movement during the drainage process using the Lattice Boltzmann method for different cases of viscosity ratios and capillary numbers. They observed that the formation of the fluid front and its transition between its different forms is strongly a function of microscopic flow patterns and invasion dynamics. They found that a low viscosity ratio causes a lower degree of saturation of the non-wetting phase at the breakthrough time (i.e., when the non-wetting fluid reaches the outlet boundary). The lower saturation level leads to a diffuse pattern of front movement and consequently leads to the breaking up of fingers into droplets. In contrast, a high viscosity ratio leads to higher saturation of the non-wetting phase as a result of the slow movement of the liquid front [4].

In addition to exploring the capillary number, viscosity ratio, and wettability parameters, some studies focused on the formation and movement of the liquid front under the effect of varying permeability. Shabina et al [5]. analyzed the capillary-driven flow of a wetting phase while displacing the non-wetting phase in a layered porous medium. They noted that in a stack of layers with different permeability values, the fluid front in the lower permeability (higher capillary pressure) layer will always lead. For example, in a three-layered porous medium, as the permeability changes from low to medium, and then to high values, the front leads in the small-permeability layer and then is followed by the front in the medium-permeability layer, which is followed by the front in the large-permeability layer. On the other hand, in a study done by Reyssat et al [6] on the imbibition process in a layered porous medium, a sharp front was observed despite the medium having layers with different permeability values in the direction of the flow.

Among all the conducted investigations, the one by Bico and Que´re´ [7] was the first to demonstrate that the liquid front, during the spontaneous imbibition of a wetting fluid into a porous medium, has two forms: sharp and diffuse. During the imbibition process with a diffusive front, the wetting phase was found to lead in the smaller pores of a porous medium, unlike the predictions of the traditional capillary-tube bundle model. Bico and Que´re´ also discovered that a large spread in the pore size distribution is the main cause of the formation of the diffusive fronts. Later, more studies were done on wicking in a different type of porous media including paper napkins, towels, diapers, and fractured oil reservoirs which observed the formation and progress of diffusive fronts

[8-10]. Ferer et al [11] showed that, unlike the large-scale multiphase flows in porous media, the saturation front displacement at small-scale flows is a nonlinear function of time and is caused by the fingering phenomena at pore-scale.

All the work listed till now pertain to some type of artificial, lab-scale, thin porous media created in a lab to study the front formation under imbibitional or displacement-type flows. In this paper series, we will concentrate on the commercial, rather-small cylindrical wicks used by industry to dispense incense or insecticide in the air. Hence the uniqueness of the present set of two paper series lies in the fact that it studies the categorization and exploration of liquid fronts formed during the wicking of liquids in *commercial wicks*. (Such cigarette-sized wicks are created from polymer beads or fibers using some type of sintering or compaction or extrusion process and are quite homogeneous compared to the ordinary lab-created porous media.)

2. CORRELATING LIQUID-FRONT TYPE WITH MICROSTRUCTURE

In the first part of this two-paper series[12], we investigated the process of wicking in a large set of industrial wicks consisting of six sintered-beads wicks and four fibrous wicks to answer some fundamental questions. The first question was: can one observe sharp liquid-fronts in all the wicks? If not, then how many of them will display a diffuse front? To answer this, a wicking experiment was conducted where a red-dyed liquid was spontaneously imbibed by the selected wicks in a vertical configuration. Overall, three categories of fronts were observed. The sintered beads wicks (B1 to B6) unfailingly showed a *sharp* front during these experiments. The first two of the fibrous wicks, F1 and F2, displayed slightly perturbed sharp fronts that were deemed to fall into an intermediate category of *semi-sharp* fronts. The remaining fibrous wicks, F3 and F4, displayed the *diffuse* fronts that were characterized by the presence of large fingers.

As we discovered in [12], the wick microstructure plays a big role in deciding whether the liquid front during wicking is sharp, semi-sharp, or diffuse. All our sintered-beads wicks showed sharp fronts, while two of the four fibrous wicks (with fibers mostly aligned with the wick axis) showing the semi-sharp fronts and the remaining two displaying the diffuse fronts. It was also observed that the porosity too plays a role, with lower porosities in fibrous wicks giving rise to semi-sharp fronts while higher porosities (accompanied with fiber clustering) in fibrous wicks leading to diffuse fronts.

Our aim here is to conduct a 2D two-phase (liquid-air) flow direct numerical simulation (DNS) in both particulate (bead-like) and fibrous microstructures after including the capillary pressure and gravity effects and to see if we can validate our earlier empirical observations about the dependence of macroscopic flow-front type on particle shape and porosity.

2-1 EXPLORING LIQUID-FRONT FORMATION DURING WICKING IN 2D POROUS MEDIA USING DNS

In the proposed numerical simulation, it is important to use a solid-phase geometry that structurally resembles the actual geometrical arrangement of particles/fibers. In this regard, there have been different scanning methods, such as Micro-CT, MRI, and SEM, which have been developed to obtain hi-fidelity geometry of the solid phase. One of the obstacles for using these methods is the difficulty of recreating a full 3D geometry due to problems such as very large memory and large disk-storage requirements. In our current investigations with the small beads and fiber radii accompanied with tiny inter-fiber or inter-bead microscale (and possibly nanoscale) void spaces, the structure of the pore region becomes complicated very rapidly, and hence the file sizes reach the gigabyte level very quickly. In such a situation, not only does the scanning take longer (and hence becomes expensive due to the high hourly usage rates of these machines), but also, the computation time surges severely. Hence in the present effort, because of these difficulties, we abstain from a full-blown numerical simulation in 3D pore space reconstructed from the micro-CT image of our porous wicks.

In our present investigation, we modeled the wicking process in a series of geometries representing porous media packed with beads or fibers. To have an accurate investigation on the formation and progression of liquid fronts, we created 7 (seven) different geometries to have a gradual transition from a porous medium created by spherical beads (circles in 2D) to a porous medium made of very long fiber-like ellipsoids (ellipses in 2D). Note that in this preliminary study, *we conduct this simulation in 2D in order to keep our memory and disk-space requirements smaller and more manageable* (as compared to a full 3D study where the number of nodes rise to the order of N^3 compared to N^2 in a 2D study).

Here we use ANSYS Fluent for modeling the two-phase (liquid-air) flow in different porous media and track the movement of the liquid-air interface representing the wicking front at the *microscopic* level. The Navier-Stokes equation is solved in a unit cell[2] representative of an idealized porous medium to predict the movement of the liquid in the pore region of the generated porous medium, while the curvatures and surface tension are used to generate the stress difference at the interface. The volume of fluid method is employed to discretize the equation sets. Since the Fluent simulations are quite ubiquitous and their physics is quite well known, the mathematical

[2] Here we have taken the unit cell to be similar to the representative elementary volume (REV) that is used to upscale phenomena in porous media from micro to macro scales in porous media. The general criterion is that there should be sufficiently-large number of particles in the REV, and the REV size should be much bigger that the size of inter-particle channels [13] S. Whitaker, *The method of volume averaging*. Springer Science & Business Media, 1998.

and computational details of this simulation are not presented here—rather they are given in the appendix.

Thus the effect of microstructure on the formation and progress of such fronts in different wicks is studied. Later we extract information about the *macroscopic* fronts traversing through our idealized porous medium, which were computed after area-averaging the distribution of liquid phase within the pore space.

3. GEOMETRICAL DETAILS OF OUR FLUENT (DNS) MODEL

To have a CFD-amenable representation of our real wick microstructures, we started with circles with diameter of 20 μm and kept turning them into longer and longer ellipses with dimensions (minor diameter*major diameter) of 20*40, 20*80, 20*160, 20*320, 20*640 and 20*1280 μm. This transition from a circle to a very long ellipse helps us to investigate the differences in the shape and progress of liquid fronts in the corresponding porous media. To consider the effect of the porosity on the formation and progress of liquid fronts, we considered two cases of 50% and 70% porosities.

In order to create the unit-cells of our idealized porous medium, we used state-of-the-art software GeoDict [14]. To generate a unit-cell that conforms to the microstructure of our porous media, we needed to input the fiber diameter, porosity, and orientation of the particles. Then GeoDict starts to randomly pack the particles inside a cube-like unit-cell. In the following sections, we will explain the created unit-cells and simulation results.

In order to import the unit-cells into Fluent and to define the boundaries (Inlet, Outlet, ellipse surface, and walls), we had to do some modifications in terms of making the unit-cells into geometries that can be imported and read by Fluent. Figure 1 shows an example of the original

GeoDict-created unit-cell and the modified unit-cell prepared for Fluent.

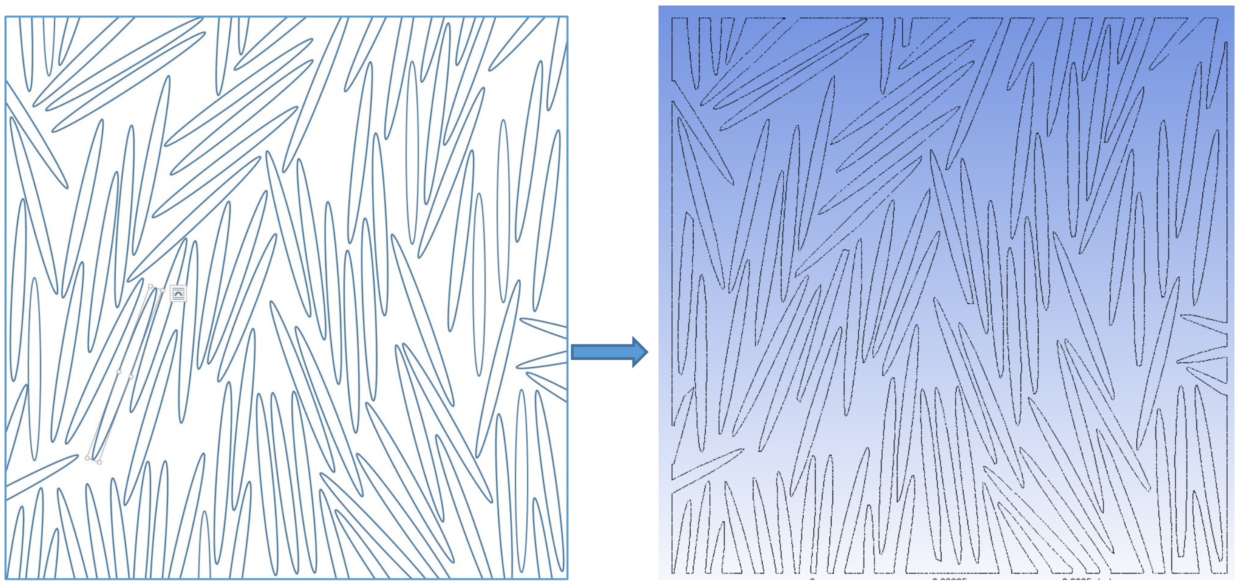

Figure 1 The process of modifying a unit-cell created by GeoDict, which is to be imported and read into Fluent. Note that the ellipse surfaces and walls are made unambiguous (for simulation purposes) in the unit-cell on the right.

6-1 Imposing boundary conditions

After preparing the geometry and importing it into Fluent, the boundaries were defined as shown in Figure 2 and the conditions applied on the surfaces are as follow:

1-0 Pa gage pressure at the inlet

2- 0 Pa gage pressure at the outlet

3- 0 degree as the contact angle between the wicking liquid and ellipses (i.e., the liquid is a completely wetting fluid)

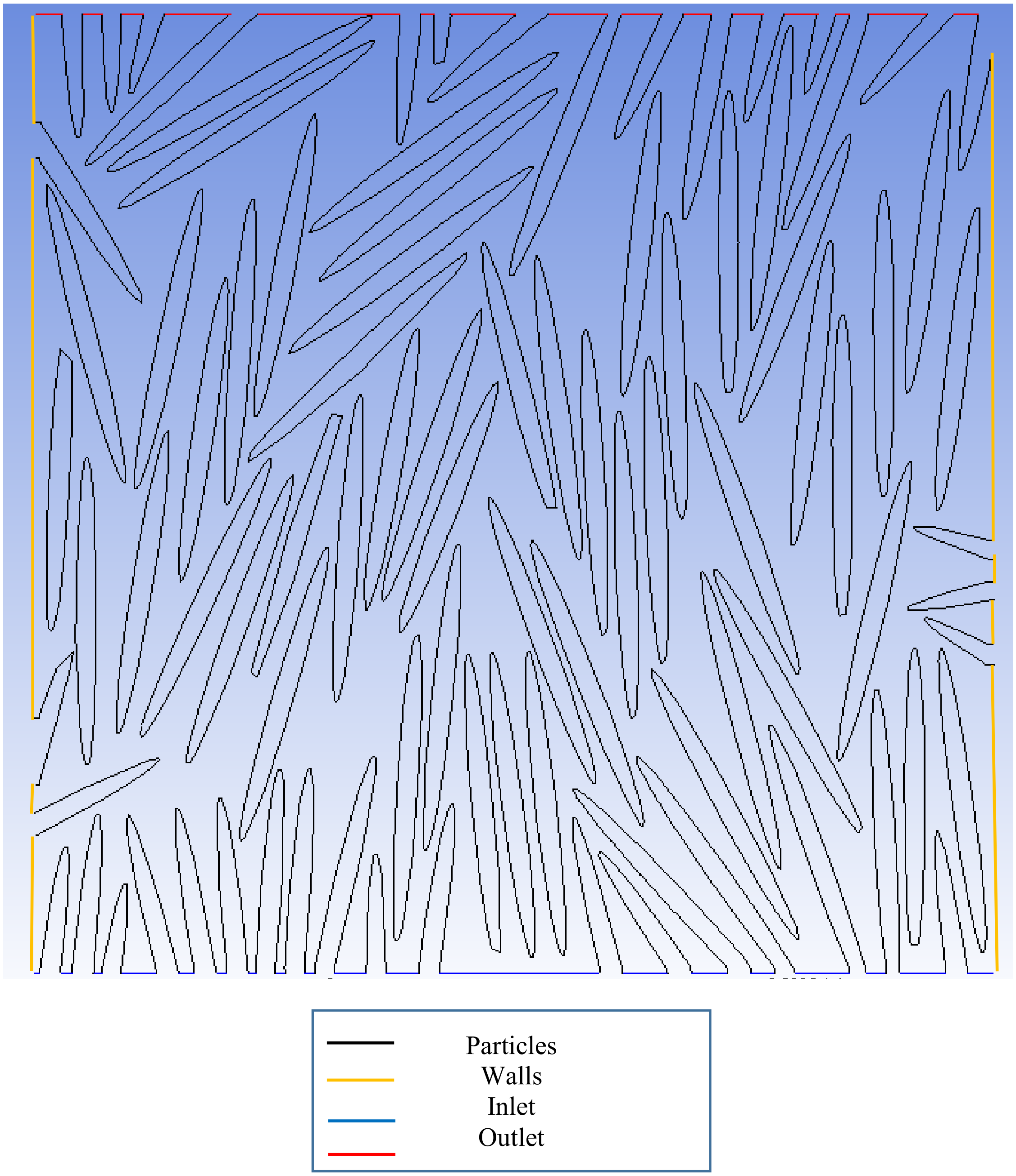

Figure 2 Boundaries shown in the color of the unit-cell geometry imported into Fluent

We conducted a mesh refinement study to acquire an optimum mesh size in order to reduce the computation time and have an acceptable level of accuracy in estimating the liquid-front formation and saturation levels. We investigated three different mesh sizes of 0.1mm, 0.01mm, and 0.001mm.

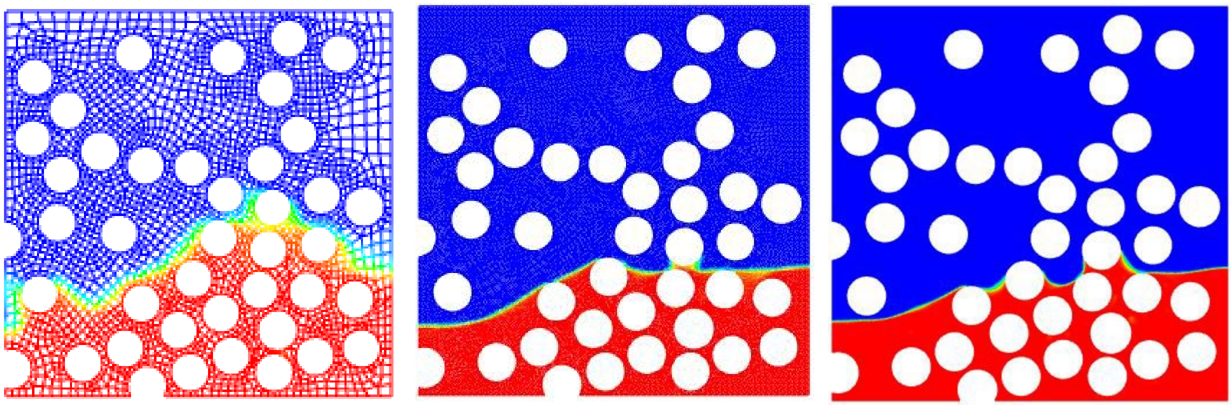

(a) (b) (c)

Figure 3 Mesh refinement study showing the mesh along with phase distributions: a typical interface during the imbibition (wicking) process at a specific time-step for the mesh size of – (a) .1 mm, (b) .01mm, and (c) .001 mm for the case of circular particles of 20 μm diameter. [The mesh in (b) and (c) can not be seen due to their increased mesh densities.]

Figure 3 depicts the effect of mesh size on a typical interface during wicking. We can see that for all the cases, the pattern of the fluid flow-front is similar. However, the cases (b) of 0.01 mm and (c) of 0.001 mm are closer. Also, the differences in the plot of saturation against non-dementionalized location for the mesh sizes of 0.01mm and 0.001 mm are negligible (Figure 4). Hence, we selected 0.01 mm as the mesh element size for our simulations.

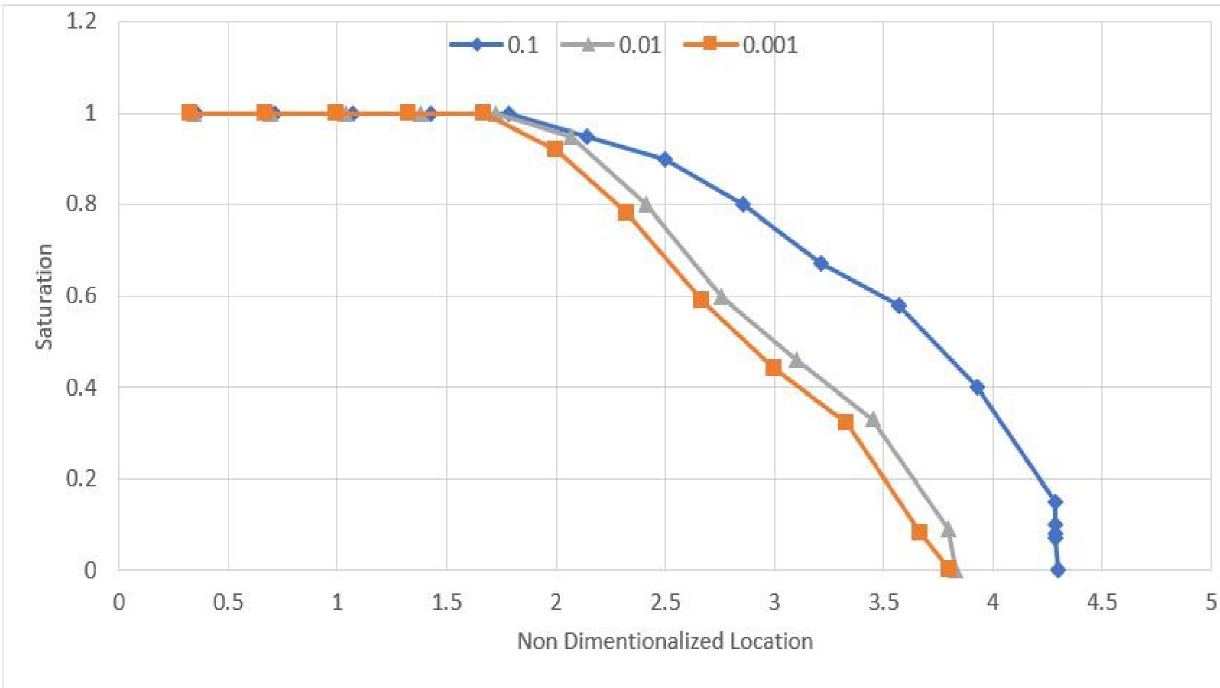

Figure 4 Plot of saturation as a function of dimensionless distance at a specific time-step for the mesh size of – (a) .1 mm (b) .01mm and (c) .001 mm for the circular particles of 20 µm diameter.

6-2 Case 1: Porosity of 50%

The first studied case was that of unit-cells packed with ellipses representing particles or fibers with a porosity of 50%. As explained earlier, GeoDict packs the unit-cells by randomly arranging the ellipses. Hence, as shown in Figure , randomly packing the unit-cells helped us to do the investigation by canceling the bias of ellipse-cluster orientations along certain directions and allowed us to be able to generalize its outcomes along the vertical (flow) direction. Figure shows the seven created unit-cells showing the gradual transition from a medium made of particles to a medium made of fibers.

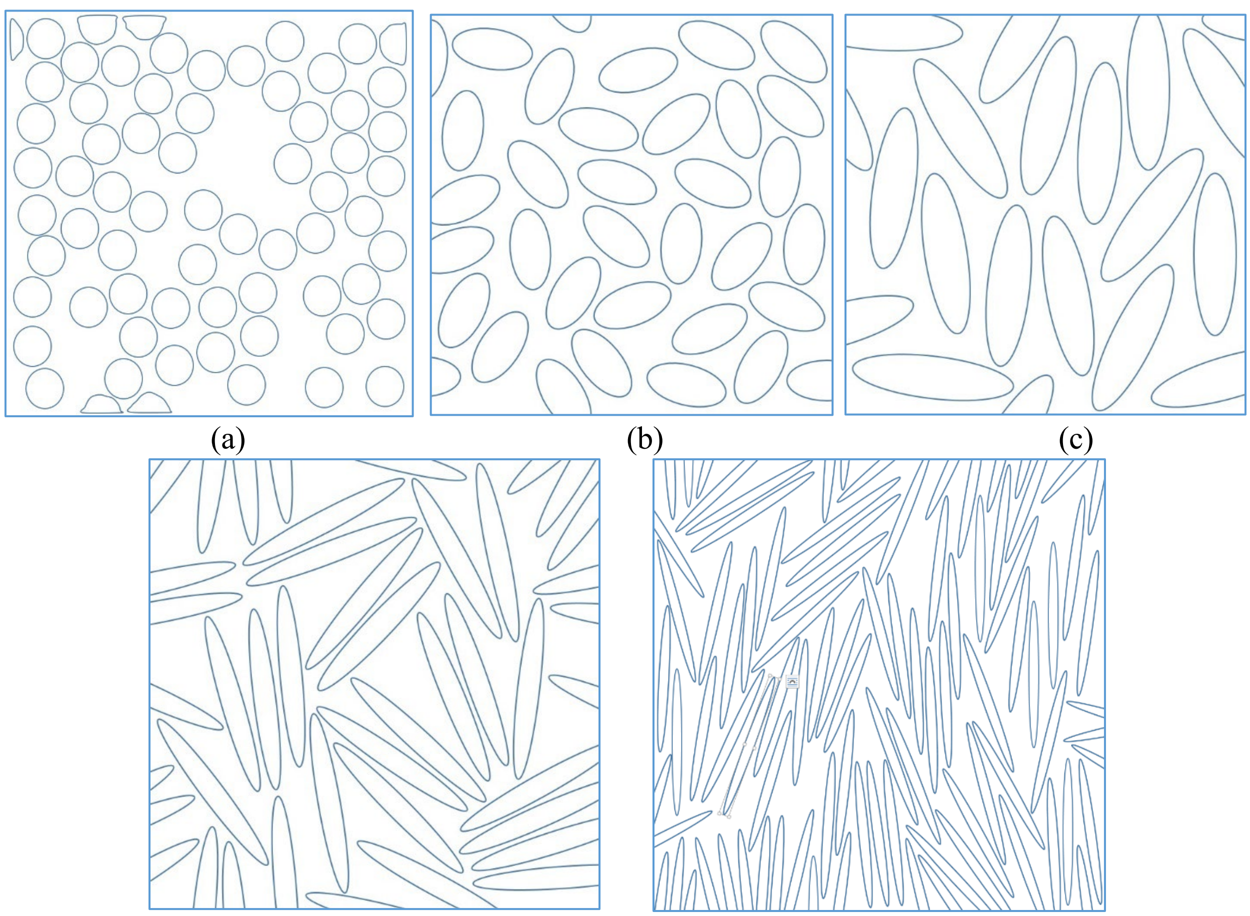

(a) (b) (c)

(d) (e)

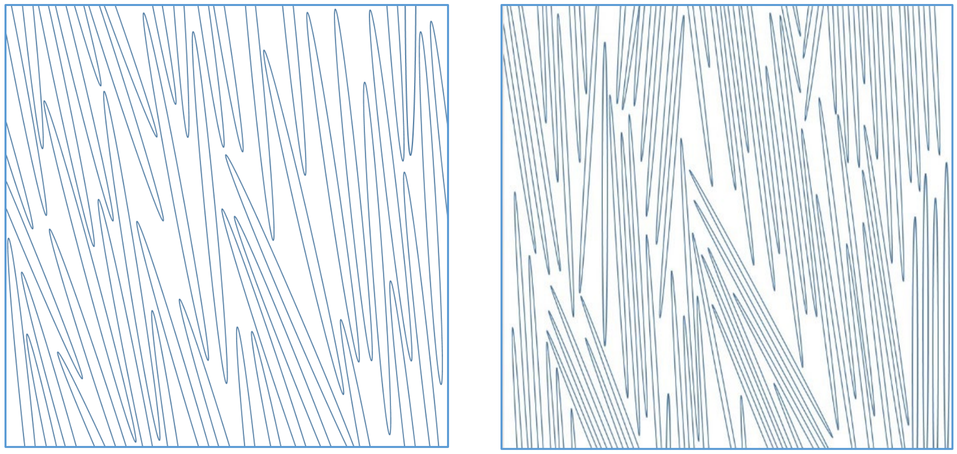

(f) (g)

Figure 5 The unit-cells created with GeoDict representing porous media at 50% porosity: the unit cells (a) to (g) show a gradual transition from a particulate porous media to a fibrous porous media. Ellipse dimensions (minor diameter*major diameter) in unit cells: a) 20*20 µm, b) 20*40 µm, c) 20*80 µm, d) 20*160 µm, e) 20*320 µm, f) 20*640 µm, g) 20*1280 µm

6-3 Case 2: Porosity of 70%

The second scenario investigated was that of porosity being 70%. Like we did for the porosity of 50%, we used GeoDict to create the unit-cells (Figure). As mentioned earlier, one benefit of having higher porosity is that we can study the effect of clustering in our simulation as well.

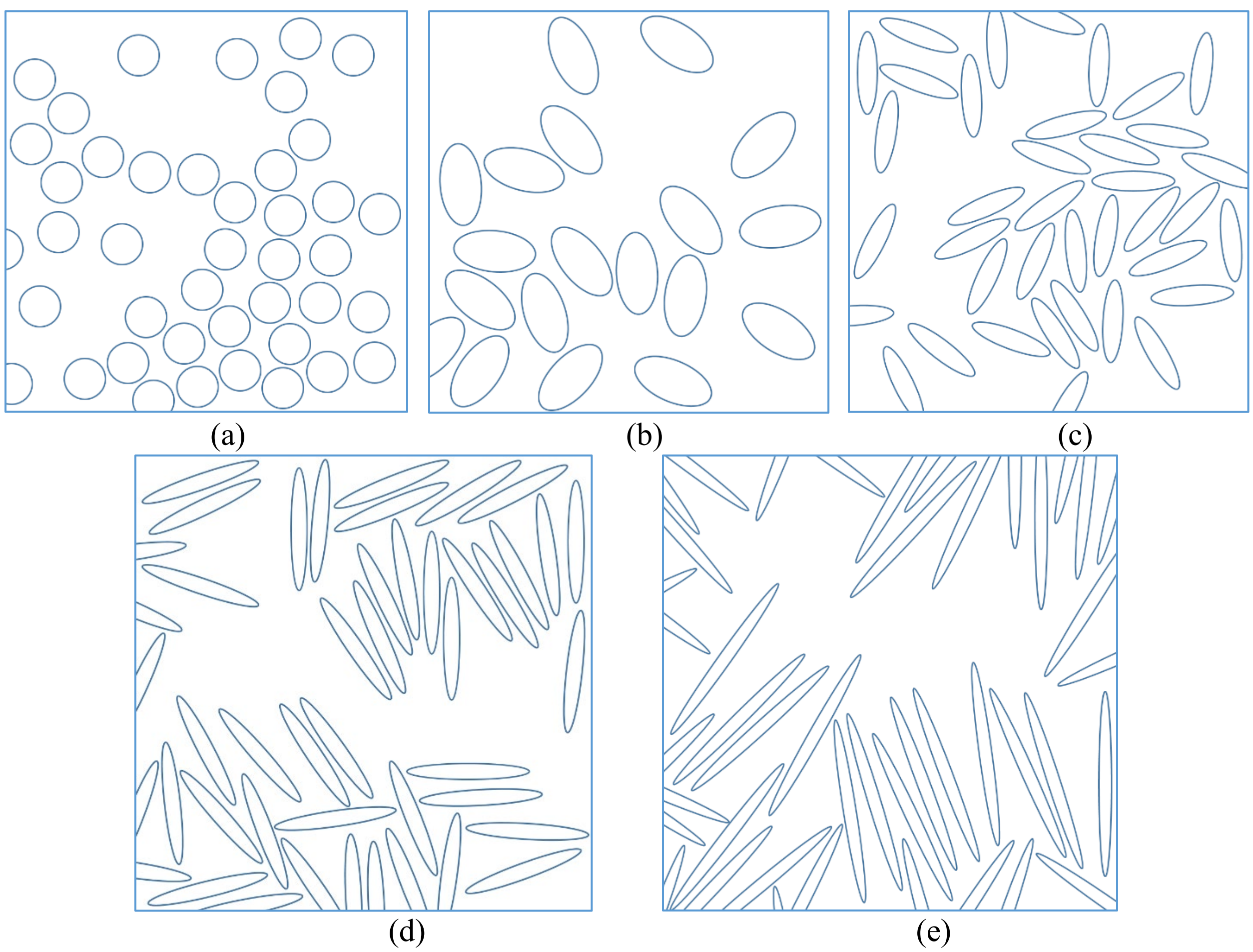
(a)
(b)
(c)
(d)
(e)

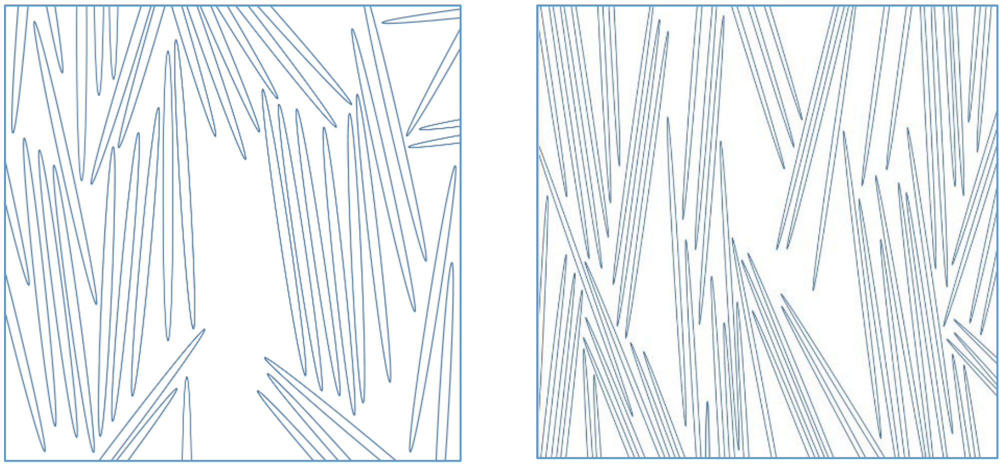

(f) (g)

Figure 6 The unit-cells created with GeoDict representing porous media at 70% porosity: the unit cells (a) to (g) show a gradual transition from a particulate porous media to a fibrous porous media. Ellipse dimensions (minor diameter*major diameter) in unit cells: a) 20*20 µm, b) 20*40 µm, c) 20*80 µm, d) 20*160 µm, e) 20*320 µm, f) 20*640 µm, g) 20*1280 µm

6-4 Discussion of Results

After importing the prepared geometries into Fluent, after applying the boundary conditions, after generating suitable meshes [15], and after activating the Fluent's multiphase module, we are finally ready to run our wicking simulations. In the following sub-sections, we present the results of the simulation; later, after interpreting them, we offer the salient conclusions.

The properties of the wicking liquid are presented in Table 1.

Table 1: Properties of the wicking liquid

	Density (kg/m^3)	**Surface Tension (mN/m)**	**Viscosity (mPa.s)**	**Contact Angle**

Wicking Liquid	931	36.16 ± 0.095	3.61±0.28	~0

6-4-1 FORMATION AND PROGRESSION OF LIQUID-WATER INTERFACE

Figure 7 and Figure 8 show the evolution with time of the interface between the wetting and non-wetting phases during the simulation of the imbibition (wicking) process for unit-cells with porosities of 50% and 70%, respectively. To have a better understanding of the formation and progress of the interface, we showed the results corresponding to three different time steps in the same geometry.

On studying the sequence of figures from Figure 7 (a) to (g), we see clearly how the front formation is influenced by the aspect ratio of ellipses at lower porosity of 50%. For the 20*20 µm and 20*40 µm ellipses, which can consider as circular or near-circular particles, we observe a somewhat flat front in the unit-cell. This means that transition from the fully wet 100% saturation to the dry 0% saturation happens over a small distance, notwithstanding the deviations caused by local heterogeneity due to clustering. This points to the fact that perhaps the front seems like a sharp front when looked at macroscopically, which matches with our experimental observation [12] that (macroscopic or visual) liquid fronts in the sintered-beads wicks are invariably sharp. On replacing the circles with ellipses of 1:4 aspect ratio (i.e., with 20*80 µm dimensions), the transition from the fully wet 100% saturation to the dry 0% saturation happens over a larger distance. This trend strengthens and the transition region becomes longer when the ellipses change to 1:8 (20*160 µm) and 1:16 (20*320 µm) aspect ratios. Then the macroscopic interface, which represents the visual liquid-front, maybe transitioning to becoming a semi-sharp front. One can witness the appearance of fingers of liquids climbing preferentially in narrower spaces, thus leading to the loss of sharpness of the macroscopic fronts. Finally, for the ellipses with higher aspect ratios of 1:32 (20*640 µm) and 1:64 (20*1280 µm), the trends become stronger of the heightening of finger formation and the elongation of the transition region. As a result, one can expect the visual front to become more and more diffuse.

A similar trend can be seen in Figure 8 (a) to (g) for 70% porosity. However, since the porosity is higher, there are more gaps in the microstructure and more evidence of clustering of 'particles' or 'fibers'. Through not much difference can be seen in the fluid distribution patterns for the three initial ellipse sizes (20*20 µm, 20*40 µm, and 20*80 µm), one can, however, observe that the length over which the local saturation changes from 100% to 0% is now a bit longer. As a result, the macroscopic front is perhaps likely to be changing from being sharp to being semi-sharp more 'easily'. For the last four ellipse sizes (20*160 µm, 20*320 µm, 20*640 µm, 20*1280 µm), the length over which the local saturation changes from 100% to 0% is now clearly longer. Hence the visual or macroscopic fronts are going to be more diffuse. In particular, a comparison of Figures 7 (g) and 8 (g) reveals that for the higher porosity case, the micro fronts are more 'broken up', have more pockets of air trapped, and extend over a longer length —clearly pointing to a more diffuse visual (macro) front.

As was summarized at the beginning of section 2, our conclusion from Figure 7 and Figure 8 reaffirms the experimental observation seen in part 1 of this paper [12] that as *the porosity increases, the liquid front type changes from sharp to semi-sharp to diffuse*. In unit-cells with the lower porosity value, the particles and fibers are closer to each other and more homogeneously distributed, and consequently, the tiny micro-fronts climb uniformly in the interstitial channels to generate a sharper macro-front.

As shown in Figure 8, as the porosity increases, there is more of a chance for particle/fiber clustering to occur, and we do observe higher concentrations of solid phase in several local areas of the microstructure. Such an existence of clustering leads to local inhomogeneities, and consequently, there is a faster motion of the wetting phase in these narrower channels. This leads to faster climbs of tiny micro-fronts in the clusters compared to the more 'open' regions, which causes the visual (macro) front to be more diffuse.

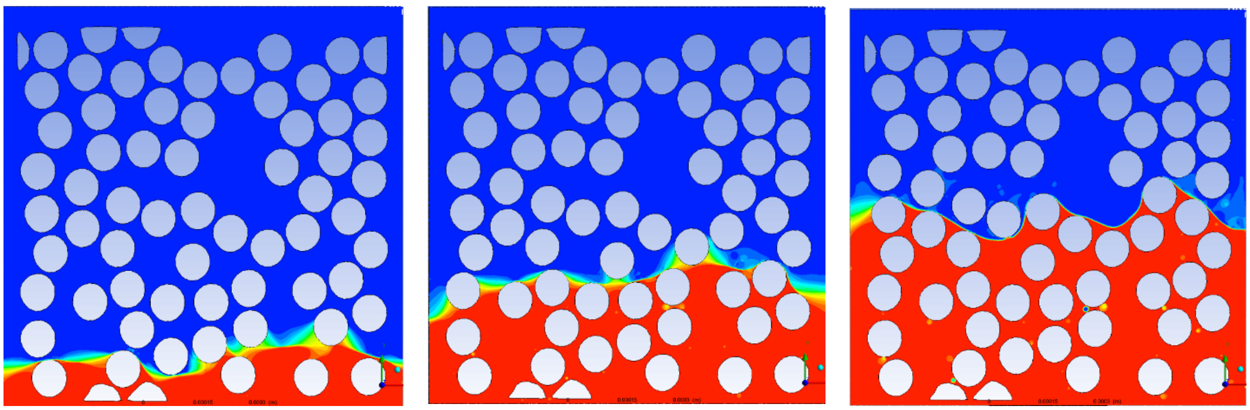

(a)

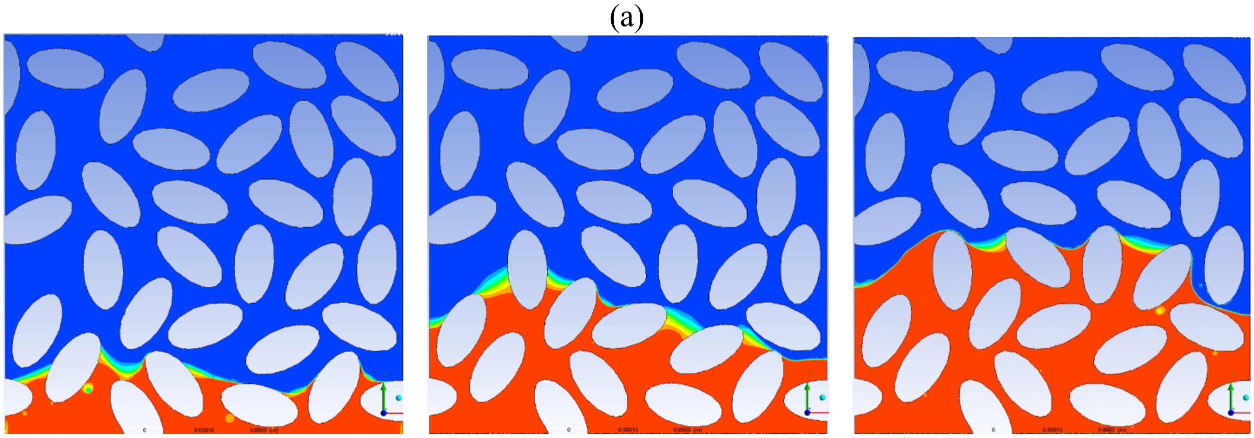

(b)

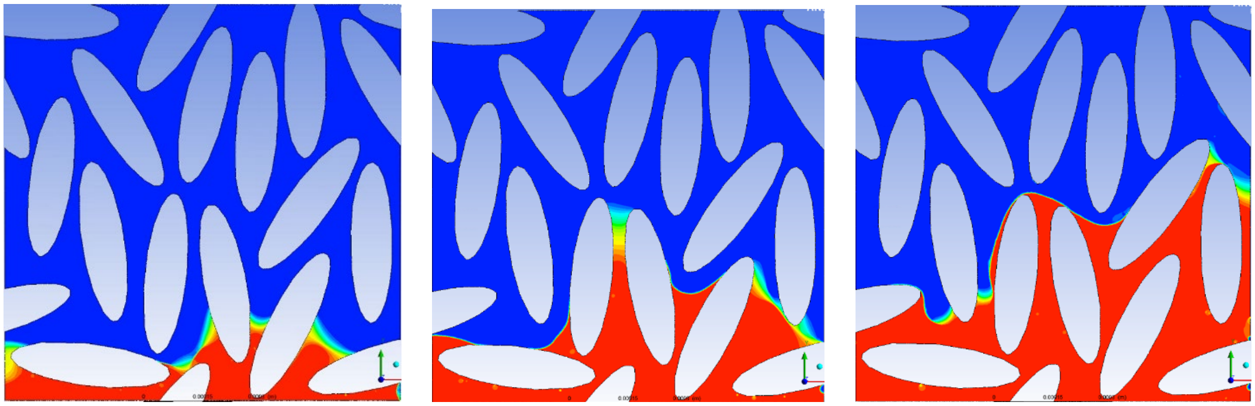

(c)

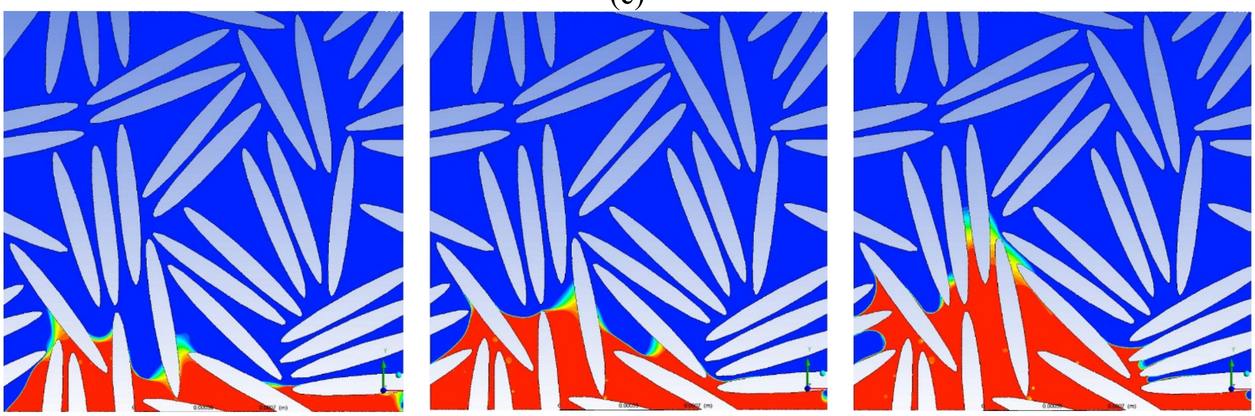

(d)

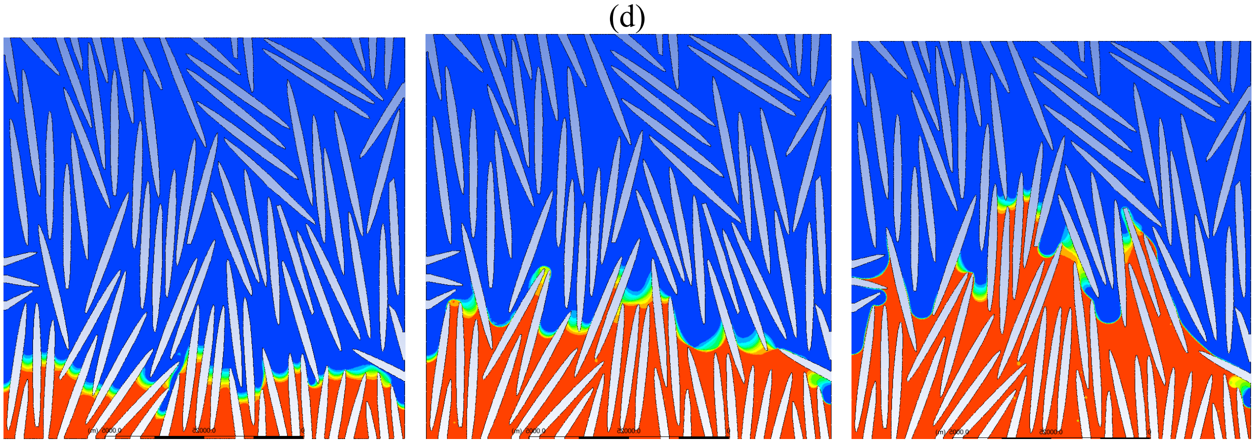

(e)

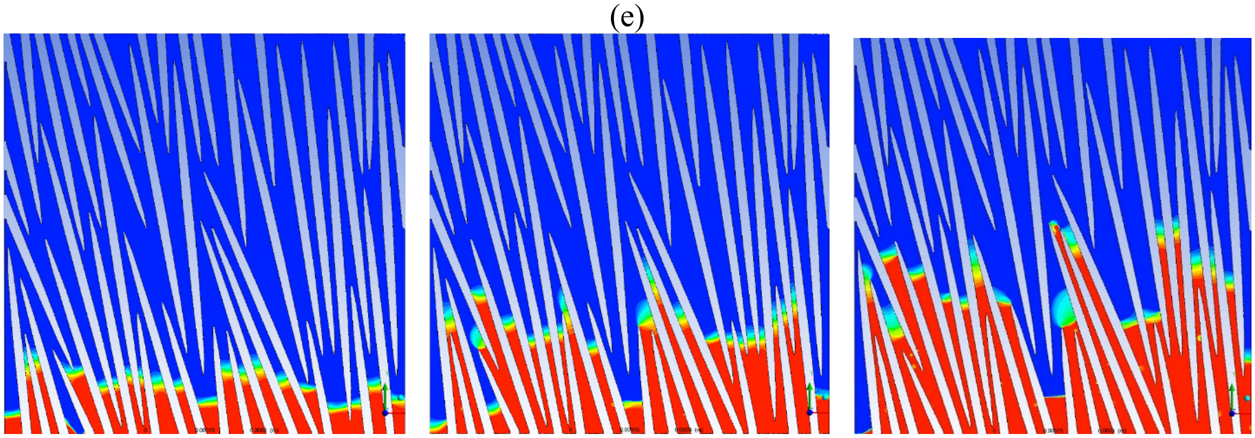

(f)

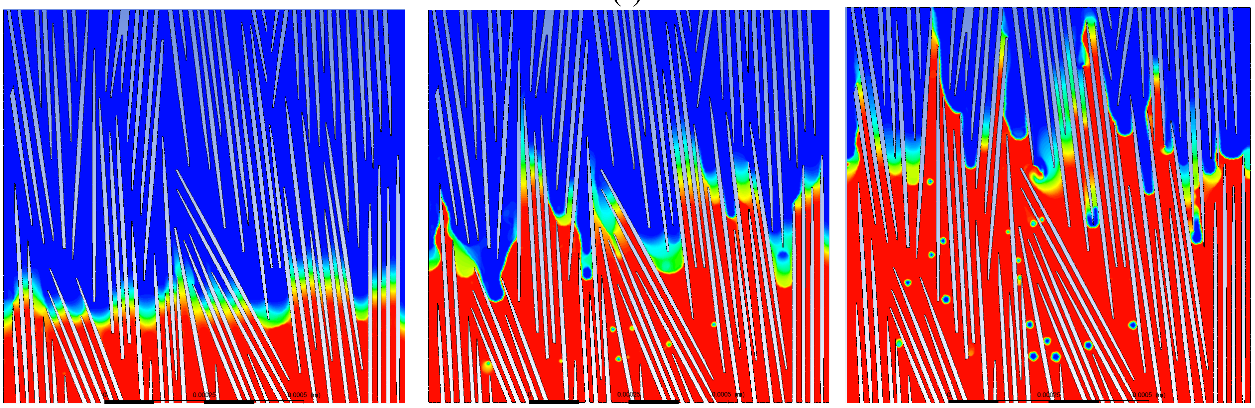

(g)

Figure 7 The movement of the liquid-air interface during the imbibition process in three different time steps in the unit-cells with a porosity of 50%. The dimensions of ellipses are: a) 20*20 µm, b) 20*40 µm, c) 20*80 µm, d) 20*160 µm, e) 20*320 µm, f) 20*640 µm, g) 20*1280 µm

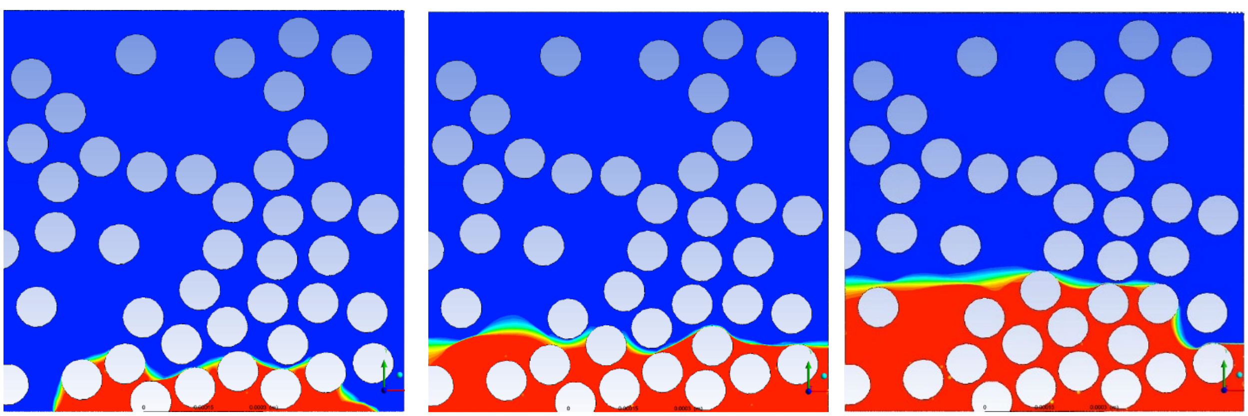

(a)

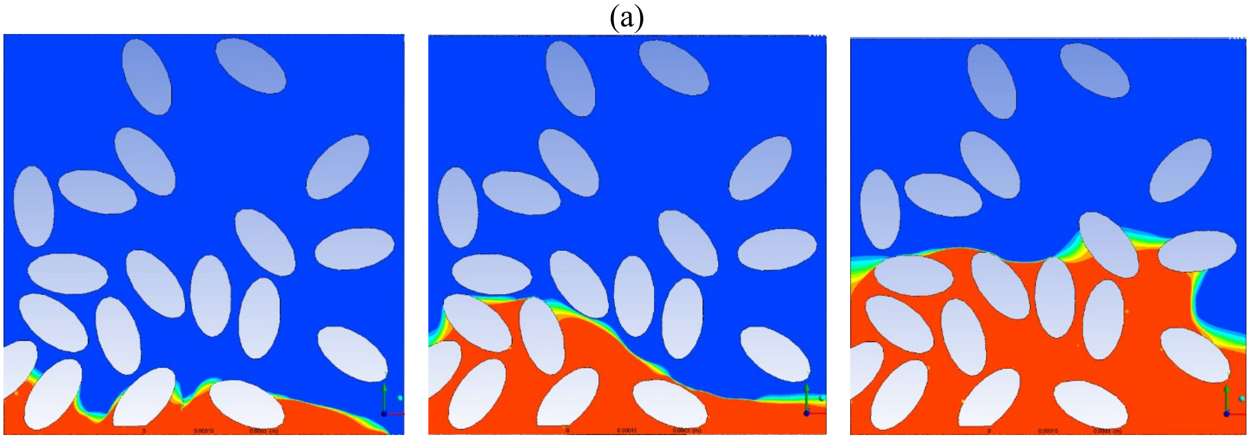

(b)

(c)

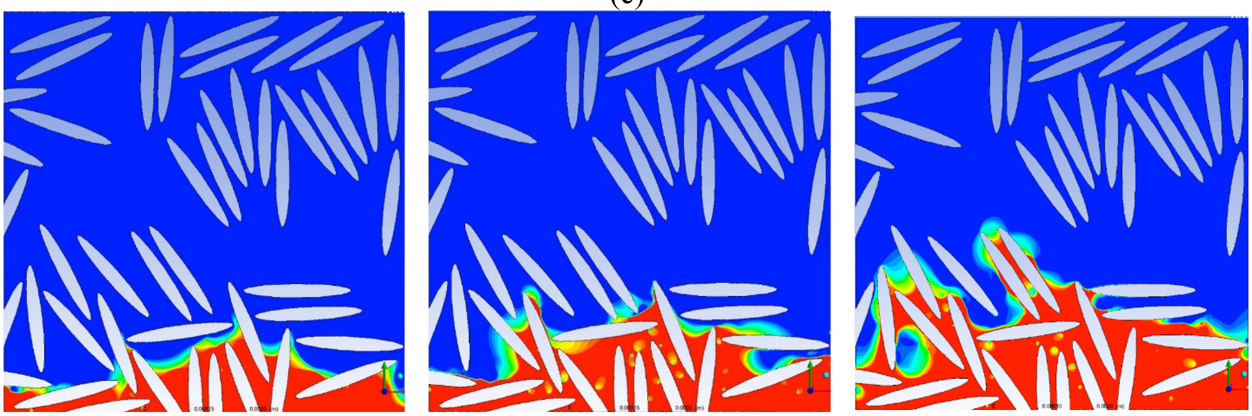

(d)

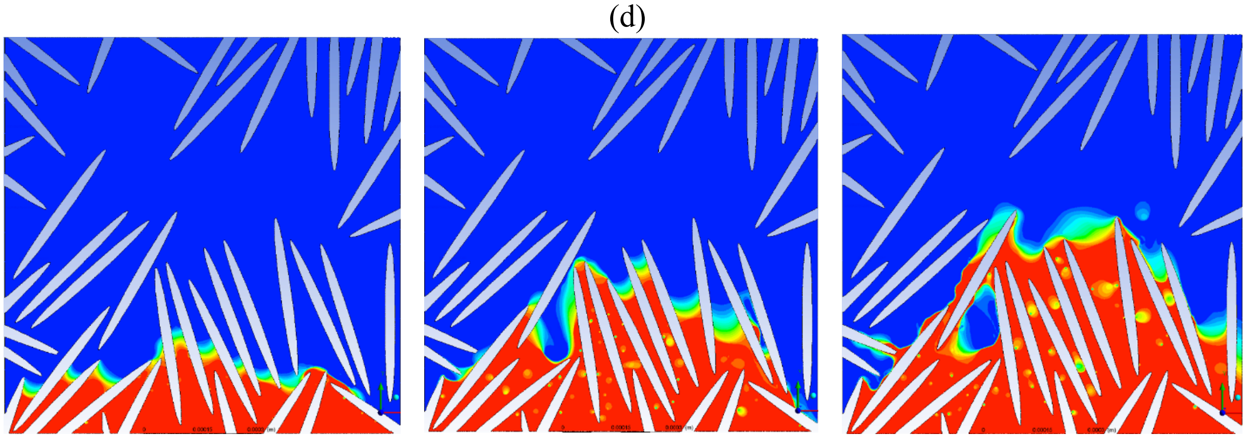

(e)

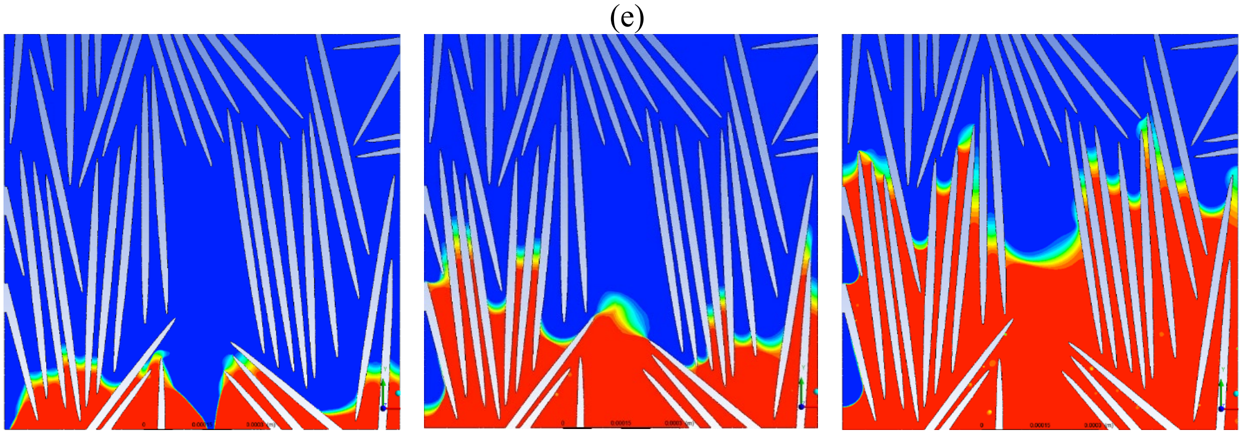

(f)

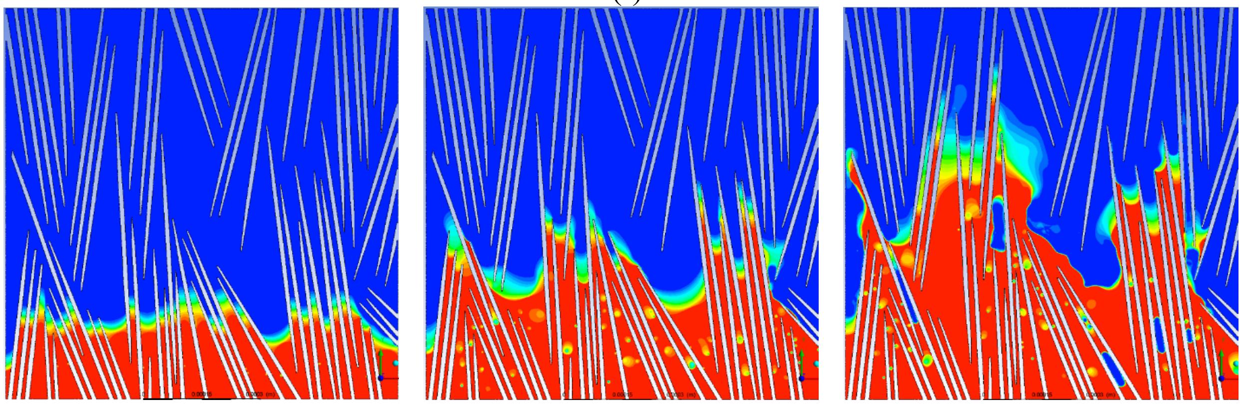

(g)

Figure 8 The movement of the interface during the imbibition (wicking) process in three different time steps in the unit-cells with a porosity of 70%. The dimensions of ellipses are: a) 20*20 µm, b) 20*40 µm, c) 20*80 µm, d) 20*160 µm, e) 20*320 µm, f) 20*640 µm, g) 20*1280 µm

6-4-2 ESTIMATING VARIATION OF SATURATION AS A FUNCTION OF POSITION ALONG THE FLOW DIRECTION

Under different conditions of the sharp and diffusive fronts, saturation becomes a function of time and position along the flow-direction coordinate. Under the sharp fronts, all the void space behind the visual liquid-fronts are filled, completely saturated with the wicking fluid at 100% saturation, whereas under the diffusive front conditions, there is no well-defined sharp front and the saturation gradually changes from 100% to 0% over a finite length. Hence, it is important to study this dependence of saturation on location and time in our CFD study also.

In order to make this comparison, we selected 5 different time steps and for each time step, by using the post-processor module of Fluent, we obtained the fluid-phase distribution images at specific liquid-front positions.

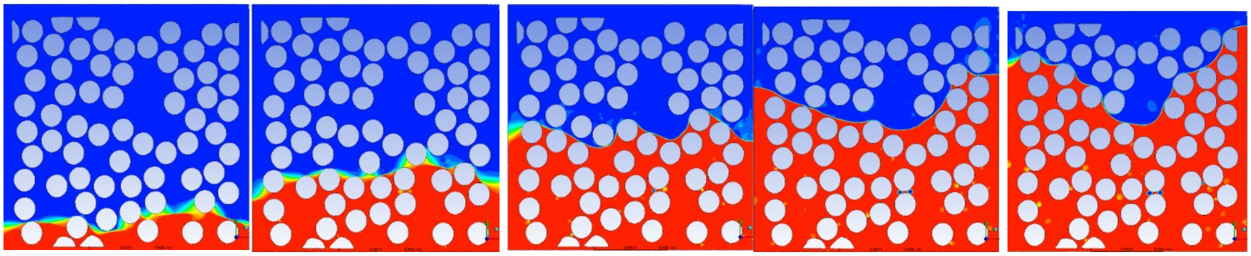

(a)

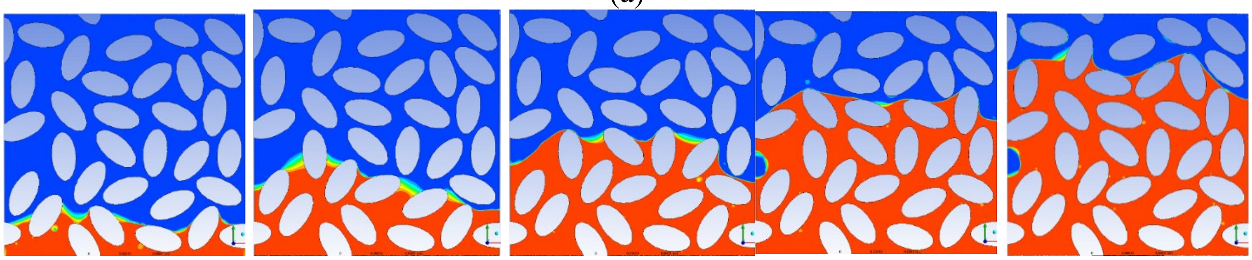

(b)

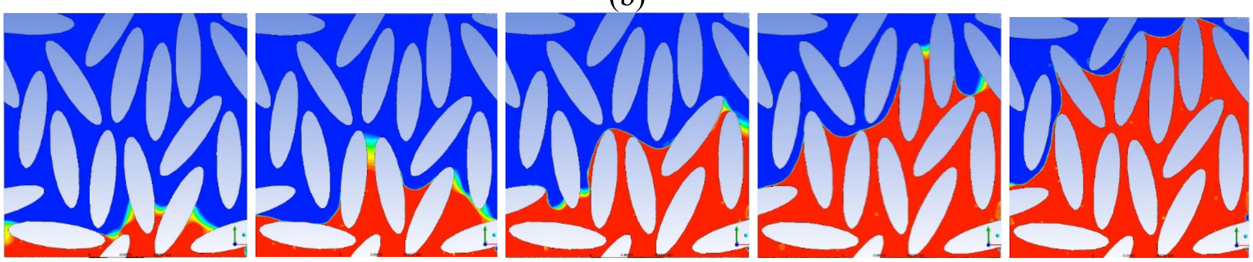

(c)

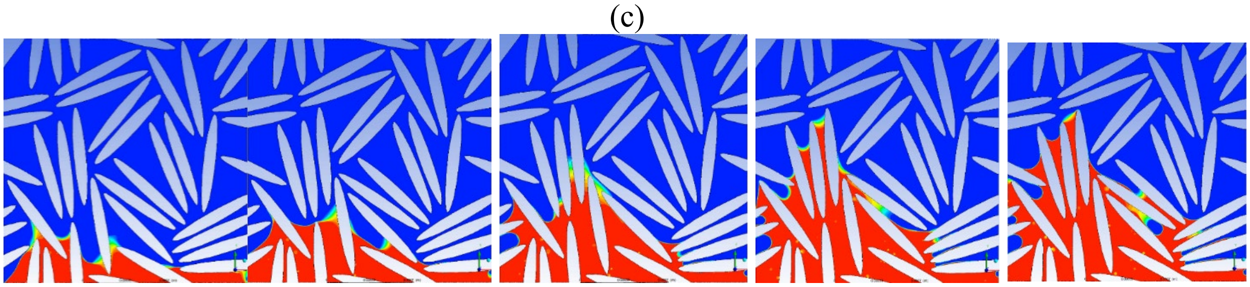

(d)

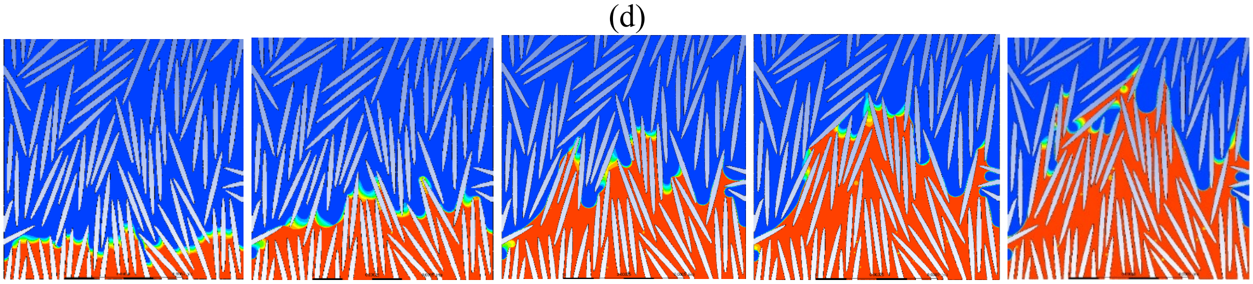

(e)

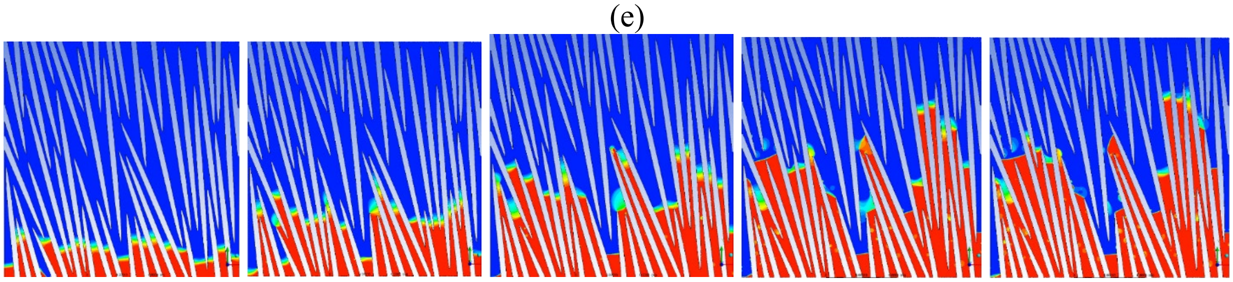

(f)

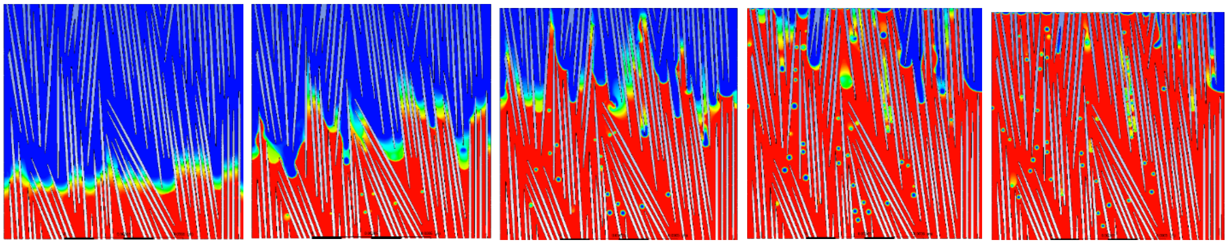

(g)

Figure 9 Five different time-steps of the wicking CFD simulation for each unit-cell having a porosity of 50 %:

*a) 20*20 µm, b) 20*40 µm, c) 20*80 µm, d) 20*160 µm, e) 20*320 µm, f) 20*640 µm, g) 20*1280 µm*

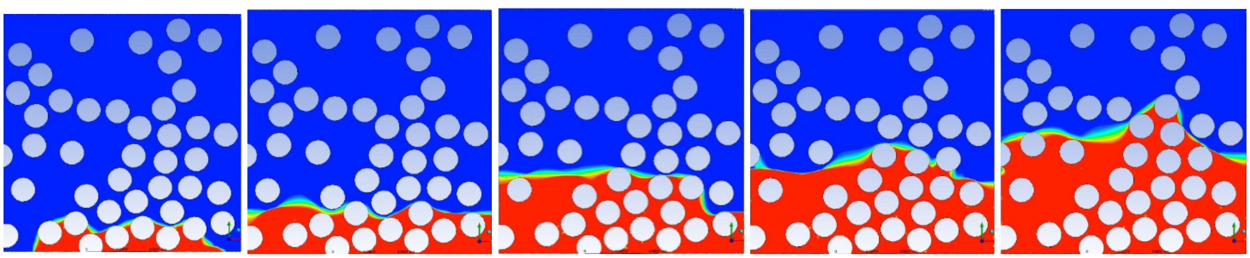

(a)

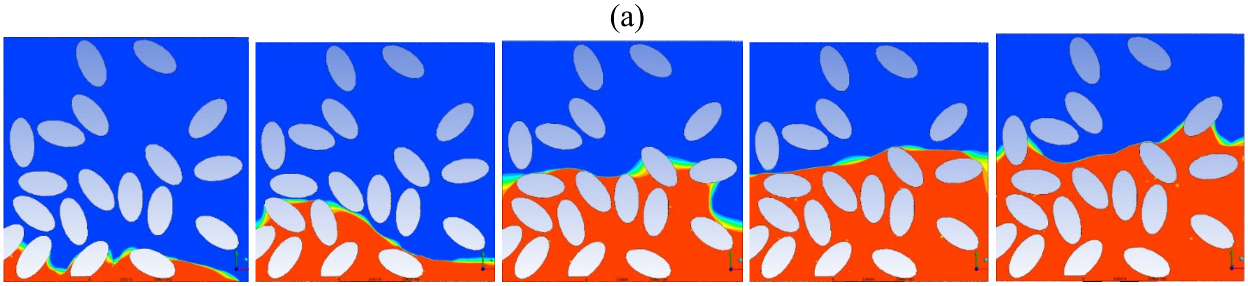

(b)

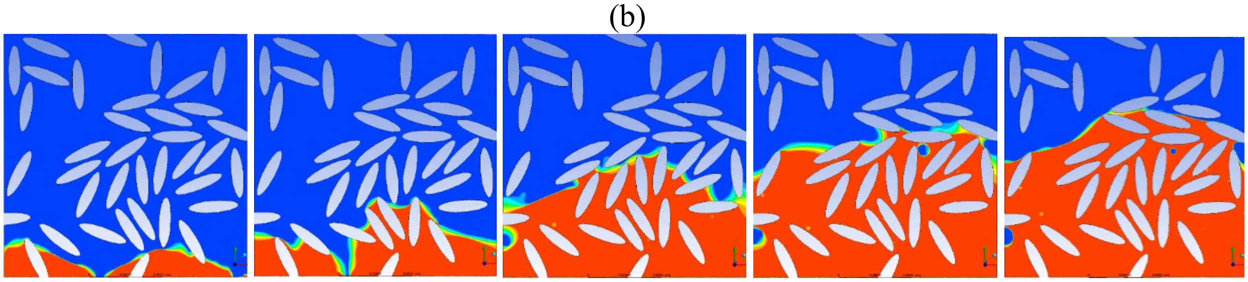

(c)

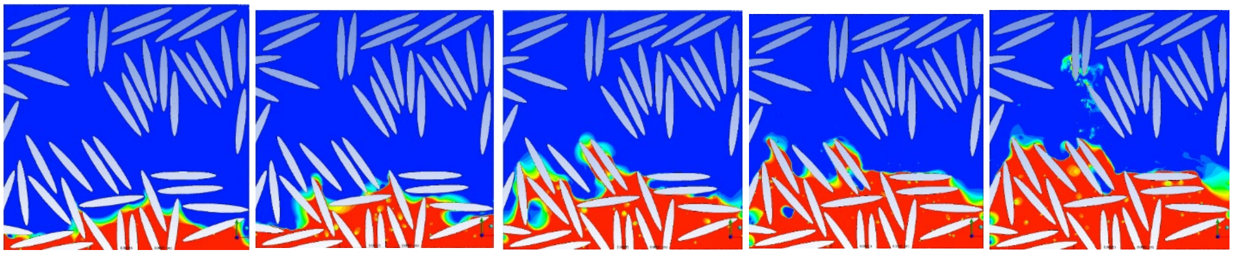

(d)

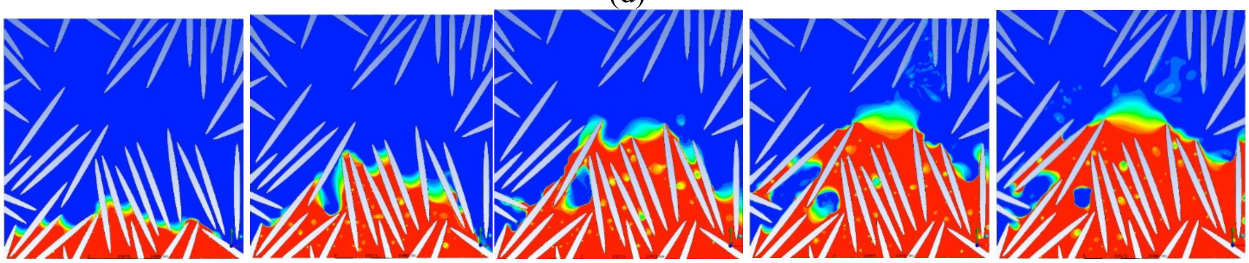

(e)

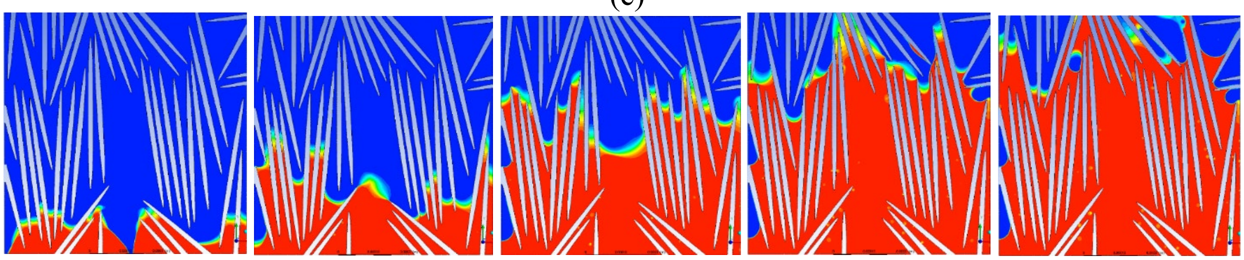

(f)

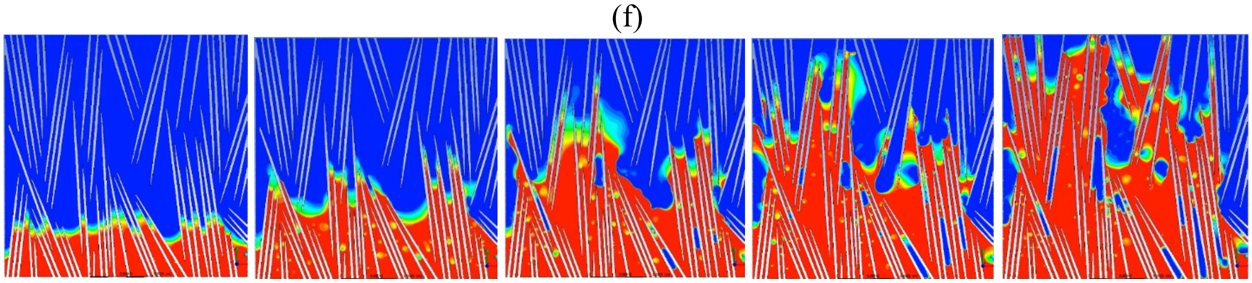

(g)

Figure 10 Five different time-steps of the wicking CFD simulation for each unit-cell having a porosity of 70 %:

a) 20*20 µm, b) 20*40 µm, c) 20*80 µm, d) 20*160 µm, e) 20*320 µm, f) 20*640 µm, g) 20*1280 µm

In the unit cells representing 70% porosity, as there is a lower number of fibers compared to the 50% porosity case, we use bigger-size unit-cells to show a better representation of the fiber and fluid distributions in these unit-cells.

In order to estimate saturation as a function of location along the flow direction, we discretize each image by superimposing a grid as shown in Figure . The grid is 25*25 and the size of each grid component is 8 micrometers.

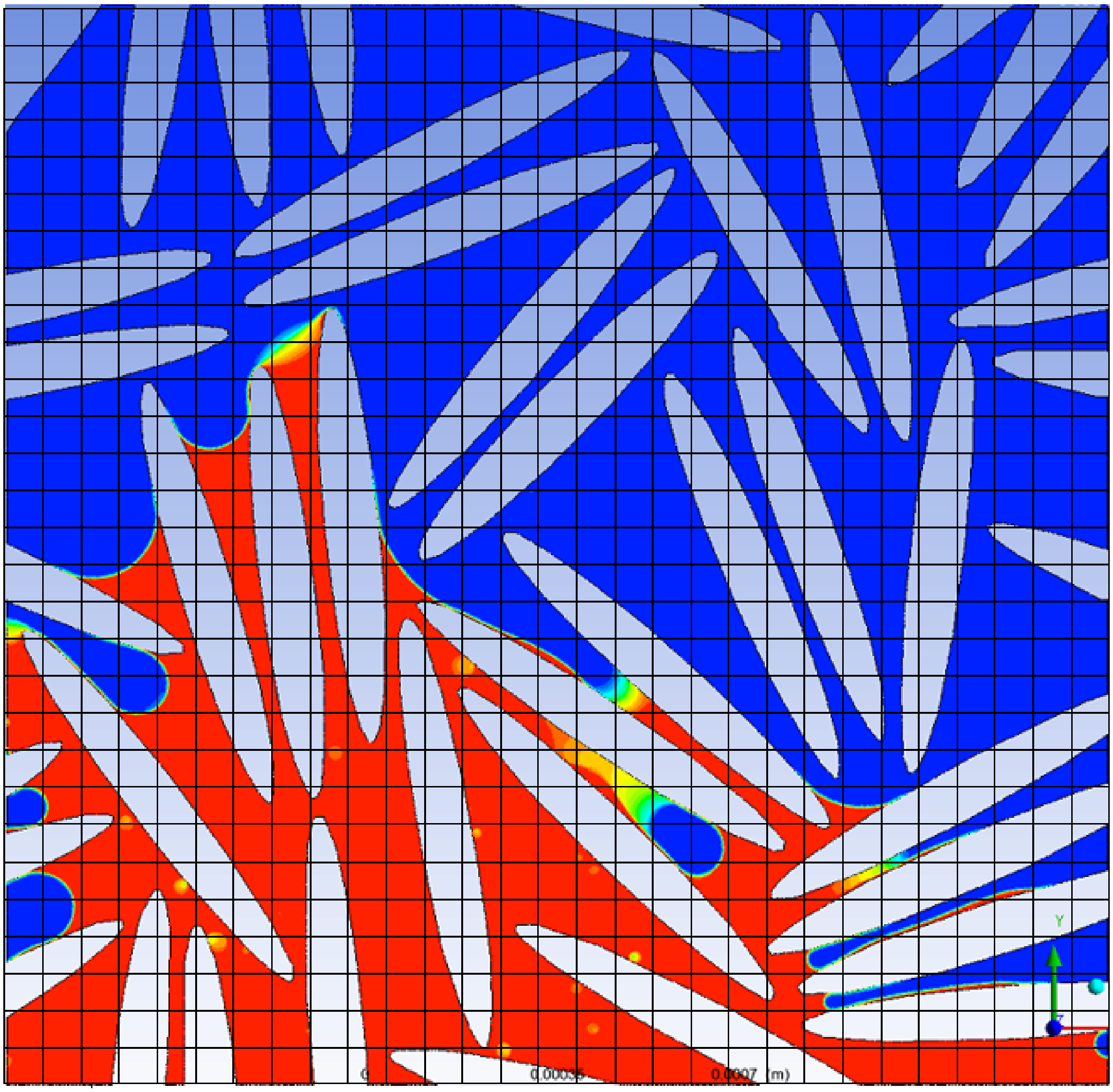

Figure 11 An example of the grid superimposed on one of the fluid-phase distribution images obtained from the Fluent post-processor module

Putting a grid on each image enabled us to compute the saturation at each horizontal row of the grid. This was done by counting the number of squares filled by the wetting phase (red color) and its ratio to the number of all squares in each row, excluding the squares containing the solid phase (white color). Hence, the sum of the squares filled with the wicking liquid as well as the number of the squares occupied by the solid phase enables us to estimate the saturation in that row as:

$$S = \frac{\text{\# of squares filled with wetting phase}}{\text{total number of squares} - \text{\# of solid phase squares}} \tag{1}$$

Calculating the number of cells filled with the wetting and solid phases was done manually. (The partially-filled squares were added with the fully filled ones to determine the total numbers for the two phases using our judgment.)Figure *3* (a to d) show the saturation as a function of nondimensionalized location ($\frac{\text{the size of each grid component or square} \times \text{the row number}}{\text{minor radius } 20\ \mu\text{m}}$) for all the five-time steps for all the seven investigated unit-cells for the investigated porosities. (The left-hand-side graphs correspond to the porosity of 50%, while the right-hand-side ones represent the porosity of 70 %.) Note that we have rendered dimensionless the distance from the entrance of the unit cells with the minimum dimension of ellipses, i.e., the radii of the circles or the minor radii of ellipses, which is 20 μm.

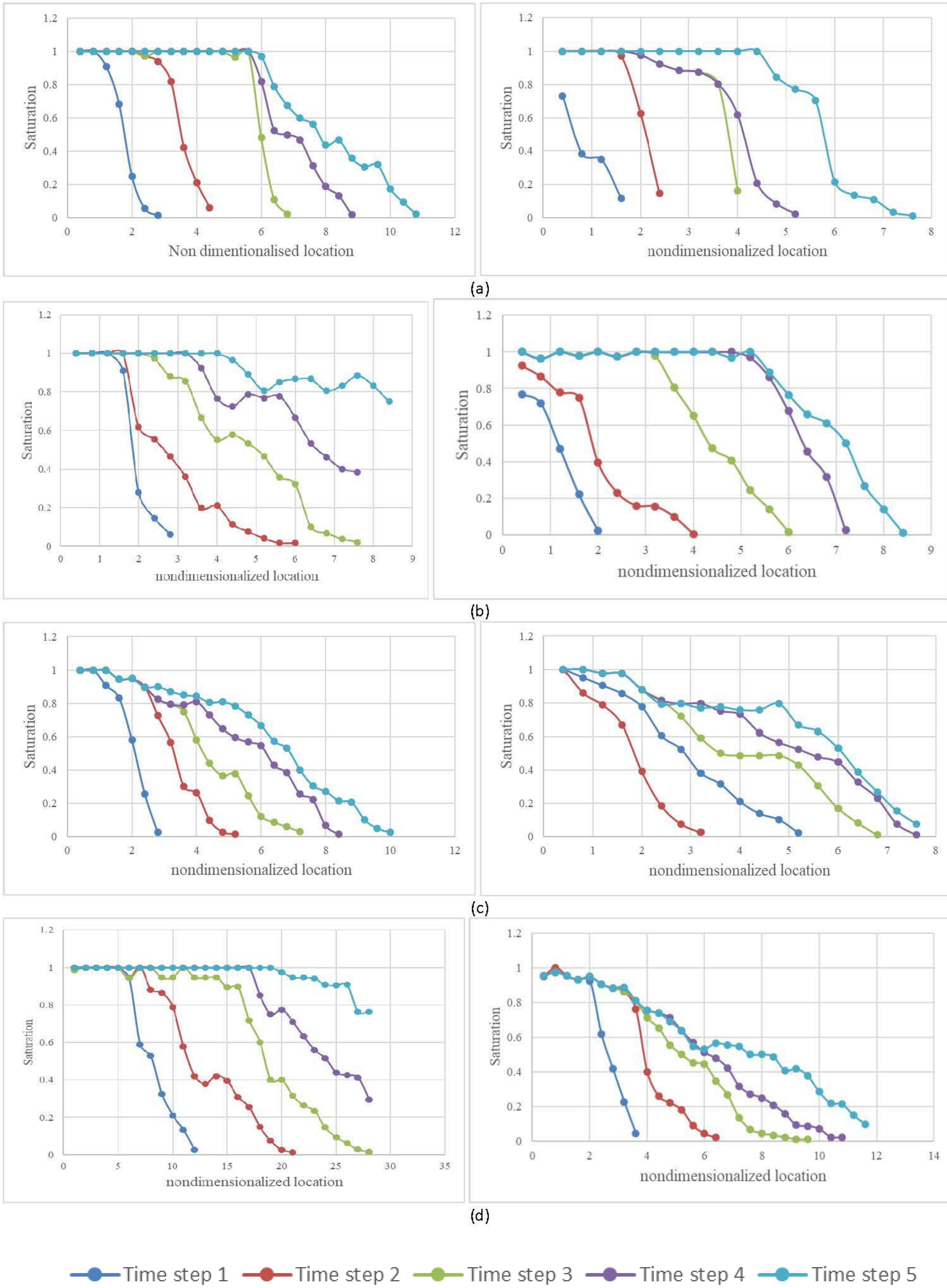
Saturation
Non dimentionalised location
nondimensionalized location
(a)
(b)
(c)
(d)
Time step 1
Time step 2
Time step 3
Time step 4
Time step 5

Figure 3 The graph of saturation as a function of the nondimensionalized flow-direction coordinate for 5 different time steps for the unit-cell packed with (a) circles of diameter of 20 μm (b) ellipses of dimensions 20*80, (c) ellipses of dimensions 20*320 and (d) ellipses of dimensions 20*1280. (Left: 50% porosity; right: 70% porosity.)

In Figure 12 a, there is less difference between the figures for the two porosities, and the corresponding fronts can be judged to be sharp. As the front-type changes to semi-sharp (Figure 12 b), which then is followed by diffuse fronts (Figure 12 c and d), the difference becomes more apparent, i.e., the liquid fronts are more diffuse and fuzzier for the 70% porosity compared to the 50 % one.

Overall, by comparing the saturation progress and evolutions shown in Figure 3 we observe that in general *by elongating the solid-phase shape [and in particular by substituting particles (circles) with fibers (ellipses)], the saturation profiles become fuzzier*.

As expected, having sharp fronts causes saturation graphs to be step-like for the unit-cells with 20*20 μm particles—as shown in Figure 3 (a), for 50% and 70% porosities, respectively. In Figure 3 (b), for the unit-cells packed with 20*80 μm ellipses, as the saturation graph starts to become fuzzy, we can infer that the macro (visual) fronts turn from sharp into semi-sharp. Later, for higher the aspect ratios of, 1:16 (20*320 μm), and 1:62 (20*1280 μm), the saturation graphs definitely grow fuzzier. As the saturation profiles move away from the sharp 100%-to-0% drops and take the fuzzier shapes, it points to the existence of a diffusive front during the imbibition (wicking) process.

Considering Figure 3 and combining it with Figure (g) gives us interesting and very important information about saturation distribution. From the two figures, one can argue that at a *lower porosity value, since there is less clustering of fibers, the saturation graph gets less fuzzy and the liquid front tends to take a less diffusive form*. In addition, Figure 3 shows the saturation levels are at high values which means that most of the grid squares are filled by the wetting phase; this is confirmed by Figure (g). In contrast, we do not observe such behavior for the unit-cell packed with ellipses of 20*1280 μm for the 70% porosity; consequences of the higher porosity are more clustering, more inhomogeneities, more micro-front formations, and finally more micro-fingers formation during the wicking process—*thus leading to clearly more diffusive saturation plots*.

In Figures 12 (c) and (d), one can also observe the *gradual diffusing* of the macroscopic (visual) liquid-fronts—the front which starts as a sharp front progressively becomes diffuse. This phenomenon was experimentally observed in Part I of the present 2-paper series [12] (see Figure 2 of that paper). Here it is clear that it is more likely to occur in fibrous media (made of high-aspect-ratio ellipses) as compared to particulate media (made of low-aspect-ratio ellipses).

The diffusing of the macroscopic (visual) liquid-fronts can also be correlated with the *front spread*, which is is the distance between the highest and lowest meniscii of the flow front. Figure 13 depicts changes in the spread for various aspect ratios as a function of square root of time. The general trend of the spread is that it increases with time. For the lower aspect ratios (ellipses of dimensions 20*20 mm and 20*40 mm, 20*160 mm) the spread is seen to be in a increasing for the first three time-steps—then, from the forth time-step onwards, it is decreasing. It is because after that time step, the upper meniscus of the flow front draws closer to the lower one. Whereas for the higher aspect ratios (ellipes of dimensions 20*320 mm, 20*640 mm and 20*1280 mm), an increasing trend is evident for all the time steps.

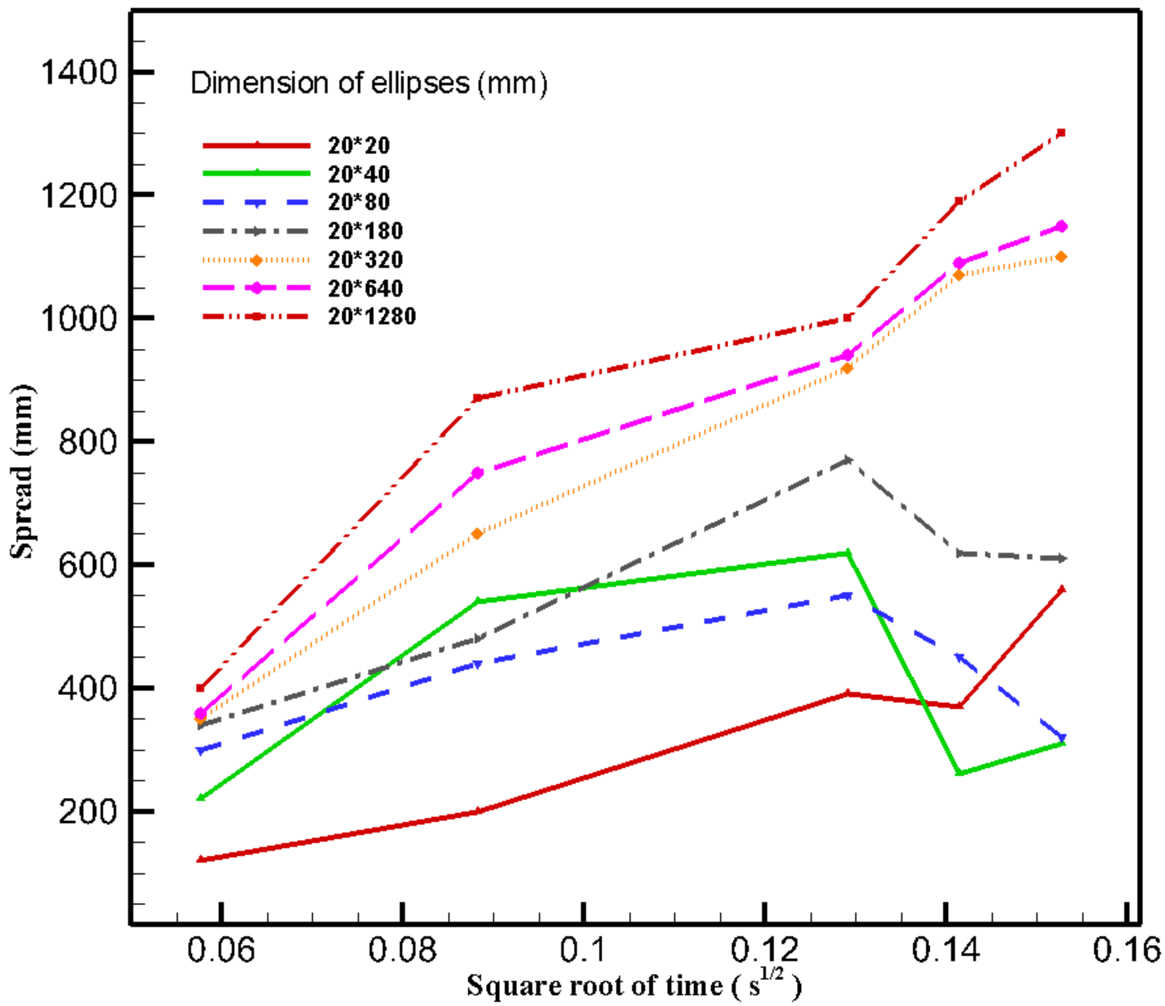

Figure 13 The graph of flow-front spread as a function of square-root of time for different aspect-ratio ellipses. The plot is for five different time-steps of the wicking CFD simulation for each unit-cell with a porosity of 70 %.

Gruener et al [16] noted that for low aspect-ratio particles,the neighbouring menisci coalesce and fuse to form a continuous flow-front displaying a low spread because of the influence of surface tension. Present study also observes that the front 'roughening' (or the spread) is only about 10-20% of the flow domain for small aspect ratios. On the other hand, for the higher aspect-ratio particles, the menisci are confined to their respective pores and are hence unable to interact with each other by an effective surface tension. Due to the lack of effective interactions between respective menisci, barriers are created between local pores. Moreover, it takes only milliseconds to fill such isolated pores with liquid. Thus, the flow front is roughened, which also correlates well with the incease in the spread seen with higher particle aspect-ratios (Figure 13).

It also worth noting that for the higher aspect ratio of particles, one can very easily fit a straight line through the spread vs square-root of time data see in this figure, which are the findings of Gruener et al [16] as well.

6-4-3 EXPLORING THE ROLE OF CONVENTIONAL DIMENSIONLESS NUMBERS

Here we will explore the question whether we could have used the typical dimensionless numbers used in previous studies involving two-phase flows in porous media [3-5, 8, 9, 11] for expressing our results.

First, we consider the Bond number which is defined as ratio of gravitational and capillary forces and is expressed as $Bo = \frac{\Delta\rho g L^2}{\gamma}$. Here, $\Delta\rho$ is the difference in density between the two phases, g is the acceleration due to gravity, L is the characteristic length, and γ is surface tension. The two fluids (air and the test liquid) were kept constant, hence their properties γ and $\Delta\rho$ were kept unchanged as well during our numerical experiments here, and in the physical experiments described in part 1 [12] . Therefore, Bo remained constant throughout our study and there was no possibility of using it as a parameter.

Next, let us consider the Capillary number, which is described as the ratio of viscous-drag forces and the forces caused by surface tension and contact angle effects. It can be defined as $Ca = \frac{\mu V}{\sigma Cos\theta}$ where σ is surface tension, θ is contact angle, μ is viscosity, and V is characteristic fluid velocity. During our physical and numerical experiments, the properties σ, θ, μ were kept constant because the fluid and wick material were kept the same. However, V could not be kept constant since the liquid-front slows down with time as it travels up in a wick. Hence it is not possible to keep *Ca* as a parameter that remains constant during the experiments.

Lastly, we consider the viscosity ratio (M) which is defined as $M = \frac{\mu_{liquid}}{\mu_{air}}$ or the ratio of liquid and air viscosities. Since the test liquid was kept the same, and the air of course was unchanged while maintaining same temperature throughout, the value of M would have been a constant during our explorations. As a result, M also could not be harnessed as an effective parameter.

Because of the unsuitability of Bo, Ca and M for serving as parameters for our study, we decided to use two geometrical factors as our parameters—one was porosity, and the other was the aspect ratio of the ellipses. They helped us to answer the question as to why different wicks display sharp, semi-sharp and diffuse flow fronts.

4. SUMMARY AND CONCLUSIONS

In this part-2 paper, we used a DNS by Fluent to model the formation and progress of the liquid front by simulating multiphase flow in the unit-cells created using ellipses. The removal of a non-wetting phase (air) by the wetting phase (wicking liquid) was successfully simulated in 2D. For our investigation, we created seven different unit-cells packed with ellipses of varying aspect ratios, starting with circular particles of aspect ratio 1 and then by increasing the ratio to represent the transition from particles to fibers. The result showed that by increasing porosity from 50% to 70%, there is an increasing tendency of the liquid front to form fingers on the microscopic fronts leading to the formation of diffusive type visual (macroscopic) fronts. Increment in porosity causes inhomogeneities in porous media due to the clustering of solid phase which leads to preferential movement of the wetting phase through narrow channels, thus leading to a 'break up' of the micro-fronts and formation of diffused visual (macroscopic) fronts. These observations broadly follow the experimental results seen in part-1 paper of this two-paper series[12], which can be listed as (a) wicks made from particles display sharper liquid-fronts compared to the wicks made from fibers; (b) the fronts in fibrous wicks become more diffuse with an increase in the porosity; (c) the fronts, especially in fibrous wicks, have a tendency to become more diffuse as they evolve in time (with the spreading of the front being proportional to the square-root of time).

5. REFERENCES

[1] W. Palmer, "28—THE ADVANCE OF A LIQUID FRONT ALONG A GLASS YARN," *Journal of the Textile Institute Transactions,* vol. 44, no. 8-9, pp. T391-T400, 1953.

[2] R. Hu, J. Wan, Y. Kim, and T. K. Tokunaga, "Wettability effects on supercritical CO2–brine immiscible displacement during drainage: Pore-scale observation and 3D simulation," *International Journal of Greenhouse Gas Control,* vol. 60, pp. 129-139, 2017.

[3] C. Zhang, M. Oostrom, T. W. Wietsma, J. W. Grate, and M. G. Warner, "Influence of viscous and capillary forces on immiscible fluid displacement: Pore-scale experimental study in a water-wet micromodel demonstrating viscous and capillary fingering," *Energy & Fuels,* vol. 25, no. 8, pp. 3493-3505, 2011.

[4] S. Bakhshian, S. A. Hosseini, and N. Shokri, "Pore-scale characteristics of multiphase flow in heterogeneous porous media using the lattice Boltzmann method," *Scientific reports,* vol. 9, no. 1, p. 3377, 2019.

[5] S. Ashraf and J. Phirani, "Capillary displacement of viscous liquids in a multi-layered porous medium," *Soft matter,* vol. 15, no. 9, pp. 2057-2070, 2019.

[6] M. Reyssat, L. Sangne, E. Van Nierop, and H. A. Stone, "Imbibition in layered systems of packed beads," *EPL (Europhysics Letters),* vol. 86, no. 5, p. 56002, 2009.

[7] J. Bico and D. Quéré, "Precursors of impregnation," *EPL (Europhysics Letters),* vol. 61, no. 3, p. 348, 2003.

[8] G. Mason and N. R. Morrow, "Developments in spontaneous imbibition and possibilities for future work," *Journal of Petroleum Science and Engineering,* vol. 110, pp. 268-293, 2013.

[9] N. R. Morrow and G. Mason, "Recovery of oil by spontaneous imbibition," *Current Opinion in Colloid & Interface Science,* vol. 6, no. 4, pp. 321-337, 2001.

[10] M. Alava, M. Dubé, and M. Rost, "Imbibition in disordered media," *Advances in Physics,* vol. 53, no. 2, pp. 83-175, 2004/03/01 2004.

[11] M. Ferer, W. N. Sams, R. Geisbrecht, and D. H. Smith, "Fractal nature of viscous fingering in two-dimensional pore level models," *AIChE Journal,* vol. 41, no. 4, pp. 749-763, 1995.

[12] M. A. F. Zarandi and K. M. Pillai, "Investigating the formation of various liquid-front types during spontaneous imbibition of liquids in industrial wicks. Part I: Experimental studies," *AIChE Journal,* vol. https://doi.org/10.1002/aic.17324, 2021.
[13] S. Whitaker, *The method of volume averaging*. Springer Science & Business Media, 1998.
[14] F.-I. G. GeoDict, https://www.itwm.fraunhofer.de/en/fraunhofer-itwm.html.
[15] M. A. F. Zarandi, "Experimental, Theoretical and Numerical Evaluation of Wicking Models for Liquid Imbibition in Dry Porous Wicks," The University of Wisconsin-Milwaukee, 2019.